Expansion and intensification of the North American Monsoon during the Pliocene

Tripti Bhattacharya,[1]* Ran Feng,[2] Jessica Tierney,[3]
Natalie Burls,[4]Scott Knapp,[4] Minmin Fu[5]

[1]Department of Earth and Environmental Sciences, Syracuse University, Syracuse NY
[2]Department of Geosciences, University of Connecticut, Storrs CT
[3]Department of Geosciences, University of Arizona, Tucson AZ
[4]Department of Atmospheric, Oceanic and Earth Sciences, George Mason University, Fairfax VA
[5]Department of Earth and Planetary Sciences, Harvard University, Cambridge, MA

*To whom correspondence should be addressed; E-mail: trbhatta@syr.edu.

Expansion and intensification of the North American Monsoon during the Pliocene

Tripti Bhattacharya,[1]* Ran Feng,[2] Jessica Tierney,[3]
Natalie Burls,[4]Scott Knapp,[4] Minmin Fu[5]

[1]Department of Earth and Environmental Sciences, Syracuse University, Syracuse NY
[2]Department of Geosciences, University of Connecticut, Storrs CT
[3]Department of Geosciences, University of Arizona, Tucson AZ
[4]Department of Atmospheric, Oceanic and Earth Sciences, George Mason University, Fairfax VA
[5]Department of Earth and Planetary Sciences, Harvard University, Cambridge, MA

*To whom correspondence should be addressed; E-mail: trbhatta@syr.edu.

Southwestern North America, like many subtropical regions, is predicted to dry in response to anthropogenic warming. However, during the Pliocene, when carbon dioxide was above pre-industrial levels, southwestern North America was wetter. While existing explanations for a wet Pliocene invoke increases in winter rain, recent modeling studies hypothesize that summer rain also played an important role. Here, we present the first direct evidence for an intensified Pliocene monsoon in southwestern North America using leaf wax hydrogen isotopes. In isotope-enabled models, warm Pliocene sea-surface temperatures on the California Margin enhanced and spatially-expanded summer convection. This mechanism is relevant for understanding future hydroclimate, since modern California Margin marine heat waves are associated with an expanded summer monsoon. Since marine heat waves are predicted to increase in fre-

quency, the future may bring intervals of 'Pliocene-like' rainfall that co-exists with intensifying megadrought in southwestern North America, with implications for human and natural systems.

Introduction

Multiple lines of evidence suggest that southwestern North America (SWNA), like many subtropical continents, was much wetter during the Pliocene epoch, a climate interval featuring reduced ice volume and pCO_2 levels elevated above preindustrial levels(Figure 1). Sedimentological data documents widespread perennial and ephemeral lakes in southern California and Arizona [1, 2] (Figure 1), and palynological and macrobotanical evidence from southern California suggests expanded tree cover and the presence of species that today only grow in regions with mesic conditions and summer rainfall [3, 4]. *Crocodylus* spp. fossils, which require freshwater habitats, are found in southern Baja California, further suggesting increased water resources in regions that are arid at present [5, 6]. At face value, this evidence for a wet Pliocene is at odds with the theoretical and model-derived prediction that regions like SWNA, and subtropical continents more broadly, will continue to dry in coming centuries as a result of elevated greenhouse gases [7, 8].

Two dominant hypotheses have been proposed to explain the evidence for wet conditions in SWNA during the Pliocene. On a global scale, a dramatically weaker meridional SST gradient could have weakened mean atmospheric circulation and reduced subtropical moisture divergence [9, 10]. However, current proxy-based estimates suggest that reductions in Pliocene meridional gradients were modest [11]. Another possibility is that a weaker Pacific Walker circulation shifted winter storm tracks, bringing increased moisture to SWNA, similar to what occurs during El Niño events today [2, 12]. However, this hypothesis would require almost two-fold increases in winter rainfall to explain Pliocene lake distributions, and cannot explain the

presence of tree species like *Castanea* and *Carya* or the expansion of Sonoran desert flora, which are interpreted as indicators of summer rainfall (*2, 4, 13*). The North American Monsoon (NAM) is the primary source of summer rainfall in the SWNA and maintains the floristically diverse ecosystems of the Sonoran Desert (*14*). Today, the NAM is restricted to southern Arizona, New Mexico and northwestern Mexico along the eastern side of the Gulf of California. However, a recent modeling study demonstrated that warmer California margin temperatures could have theoretically expanded and enhanced summer convection in the Pliocene (*15*).

Here, we present the first continuous Plio-Pleistocene record of hydroclimate from the NAM domain based on leaf wax biomarkers in a marine sediment core, DSDP 475, located off the southern tip of Baja California (Figure 2). The hydrogen isotopic signature of terrestrial plant epicuticular waxes (δD_{wax}) reflects the δD signature of precipitation (δD_p) across a range of ecosystem types (*16*). Carbon isotopes provide complementary information by recording shifts in ecosystem composition that influence the magnitude of the offsets between δD_{wax} and δD_p (Figure S1). Using paired measurements of leaf wax hydrogen and carbon isotopes, we infer Plio-Pleistocene changes in the hydrogen isotopic composition of precipitation (δD_p) (see Materials and Methods). Previous work has shown that δD_{wax}, and consequently δD_p, records the relative contribution of monsoon rainfall to annual totals in the SWNA (Figure S2) (*17*). This proxy is therefore well-suited for investigating whether summer rainfall played a role in driving Plio-Pleistocene hydroclimatic change.

Results

The leaf wax record from DSDP 475 documents a sharp transition in δD_p across the Pliocene-Pleistocene transition. Late Pleistocene values of δD_p are approximately $-65\,‰$ (Figure 2). In contrast, middle Pliocene values of δD_p range between -45 and $-35\,‰$, 20 to 35 ‰ more enriched than late Pleistocene values. The most enriched values of δD_p occur between 3.5 and

3

2.9 Ma (Figure 2), after which inferred δD_p values progressively decline. The steepest decline in δD_p occurs between 2.9 and 2.4 Ma, coinciding with the intensification of Northern Hemisphere glaciation (Figure 2). The lowest values in the record occur between 2.0 and 1.25 Ma, after which time there is a slight increase in δD_p, as well as an increase in variability. Increasing late Pleistocene variability may reflect glacial-interglacial cycles, since the presence of continental ice on North America has been demonstrated to influence NAM strength (17).

We interpret the enrichment of δD_p in the Pliocene relative to late Pleistocene values as reflecting greater proportion of convective summer rainfall during the mid-Pliocene. Summer monsoon rainfall forms from vapor that is rapidly lifted from a warm, saturated boundary in strong convective updrafts. This results in an enriched isotopic signature relative to spring or winter rainfall, which tends to be more stratiform in nature and may originate from distant sources (18). Enhanced deep convection near Baja California can therefore explain a more positive leaf wax δD_p signature during the Pliocene. Other processes, like equilibrium temperature effects, are too small to explain the full magnitude of the δD changes (see Methods), suggesting that the majority of the signal reflects enhancement of monsoon convection. In the present climatology, Baja receives less than 1 mm/day of rain on average, and in many years receives no monsoon rainfall (19) (Figure S3). Modern leaf wax δD_p at site 475 therefore reflects a mixture of waxes from the core monsoon domain and Baja California, resulting in a relatively depleted isotopic signature. In contrast, more positive Pliocene leaf wax δD_p signature at DSDP 475 likely reflects intensification of the monsoon in its core region as well as its expansion into Baja. Previous qualitative inferences from palynological data and faunal remains, which suggest that the Pleistocene marked a transition from summer-wet to summer-dry environments in southern California and Baja (4, 6, 13), corroborate this interpretation. Together, these lines of evidence suggest a stronger monsoon that influenced regions stretching from Baja California through southern California. Moreover, evidence for a warmer and wetter climate in the NAM region

4

is also shown by paleo-botanical evidence from the Miocene (*20*), suggesting this mechanism may be applicable to understanding other warm climate intervals.

Discussion

Pliocene Climate Reorganization in Southwestern North America

Alkenone paleotemperature records suggest that SSTs in coastal SWNA were dramatically warmer than present, including at DSDP 475 (*21–24*). A recent modeling study suggests that warming of coastal waters in the California margin resulted in the expansion of summer rain in Pliocene SWNA (*15*). This finding is consistent with the 'warmer-get-wetter' paradigm, which posits that the largest increases in precipitation co-occur with regions with the warmest SST anomalies, especially in the tropics (*25*). This mechanism has also been shown to play a role in future simulations of the NAM in models (*26*). To assess the Plio-Pleistocene relationship between coastal warming and monsoon rainfall, we compare our δD_p reconstruction to an index of southern California margin SST anomalies. This index is positive when this region is warmer than present day, while zero values indicate modern climatological SST values.

Between 3.5 and 3.0 Ma, the southern California margin was much warmer relative to present day. From 3.0 to 2.0 Ma, the margin cooled by approximately 7 °, reaching modern values (e.g. crossing zero) by approximately 2.1 Ma (Figure 2). This cooling coincides with a transition to more depleted δD_p values at site 475. The strong relationship between California Margin SST and monsoon strength is further corroborated by the fact that the δD_p record from site 475 exhibits the highest linear correlations with alkenone paleotemperature records on the southern California margin (Figure S4). Despite the strong relationship between these records, the reduction in NAM intensity over the Pliocene-Pleistocene transition is more abrupt than the cooling on the California Margin. This may reflect a non-linear response of monsoon strength to an SST threshold. Alternatively, it could reflect the additional influence of atmospheric changes

on the NAM. Specifically, growing Northern Hemisphere ice cover, which shifted the westerlies southward (*27*), would have promoted the 'ventilation' of the the monsoon domain with cold, dry air, reducing the energy available for convection (*17*).

NAM changes in an Isotope-Enabled Simulation

To further establish the relationship between coastal warming and SWNA precipitation, we performed two simulations with the isotope-enabled version of the Community Atmospheric Model, 5 (iCAM5). One simulation uses SST fields from (*15*), which uses PRISM3 SSTs (*28*), but prescribes additional warming on the southern California margin (Figure S5). The other simulation uses a reduced space reconstruction of Pacific SSTs based on alkenone paleotemperature records (*11*) (see Methods). Both simulations produce increases in summer rainfall, as well as enriched δD_p anomalies (Figure 3).

When forced with warmer California Margin SSTs from (*15*), iCAM5 produces a region of positive vapor δD anomalies that are co-located with warm SST anomalies. These vapor anomalies then roughly coincide spatially with enriched δD_p anomalies (Figure 3). Because SST anomalies in the PRISM3 dataset are muted south of Baja California, δD_p is slightly depleted in that region, differing from our record from site 475 (Figure 3, Figure S5). However, this simulation still illustrates the linkages between SST, vapor and precipitation δD, and summer rainfall.

When forced with a reduced space reconstruction of Pacific SST, which features warm coastal temperatures along the California margin as well as positive SST anomalies south of Baja California, iCAM5 produces a 10 to 20 ‰ increase in the isotopic signature of precipitation in western Mexico and southern California (Figure 3). This falls within the range of the reconstructed δD_p anomalies from DSDP 475 (Figure 3). Like the idealized simulation, this experiment also suggests that changes in δD_p strongly resembles spatial changes in the isotopic

6

signature of vapor (Figure 3). Both simulations are consistent with the 'warmer-get-wetter' paradigm since they show that the largest subtropical precipitation anomalies are located close to the warmest SSTs (*25*).

In iCAM5, water vapor and precipitation δD act as a tracer of changes in energy for convection. We measure the latter using equivalent potential temperature or θ_e, a thermodynamic quantity that integrates information about the temperature and moisture content of air parcels. Vertical gradients of θ_e therefore measure the potential for instability and convection. In both simulations, vertical profiles of the atmosphere over the NAM region show that positive θ_e anomalies, which imply greater potential for convection, are co-located with increases in water vapor δD (Figure 4). This is because warmer coastal SSTs drive higher evaporation rates and sensible heat fluxes, resulting in positive anomalies of θ_e. Simultaneously, coastal warmth drives enrichment of the hydrogen isotopic ratio of vapor δD, changing the signature of δD$_p$. Changes in water vapor may dominate the response in iCAM5 because model is known to underestimate δD$_p$ changes that result directly from changing proportions of convective rainfall (*29*).

These iCAM5 simulations confirm that warm California margin SSTs are responsible for stronger summer rainfall and enriched δD$_p$. Taken together with floral and faunal evidence suggestive of summer rain, our results show that wetter conditions in SWNA during the Pliocene were at least partially driven by an increase in summer rainfall, rather than solely by changes in winter storm tracks (*2, 12*). Given that a warmer troposphere would have increased evaporative demand especially in summer (*30*), summer rainfall may have been especially critical for sustaining high lake levels and perennial freshwater across SWNA.

Implications for Current and Future Southwestern Hydroclimate

Pliocene proxy evidence and model simulations underscore the linkage between California Margin temperatures and NAM strength, with implications for understanding past and future

climate in this region. Given the critical importance of coastal temperature patterns to NAM variability, climate models with significant northeast Pacific SST bias may not produce reliable future predictions (*31*). This contributes to the lack of robust predictions of future changes in the NAM, which tend to be highly dependent on model bias and resolution (*14, 32–35*). Indeed, a bias-corrected global model shows robust decreases in monsoon rainfall across all seasons (*26, 36*), in contrast to previous work (*14, 33*). This result is due in part to *reduced* California margin warming compared to the tropical eastern Pacific (*26, 37*). This mechanism of future NAM changes resembles, yet is opposite in sign, to what we propose occurred during the Pliocene. This may reflect the fact that Pliocene ocean temperate patterns reflect long-term adjustments of deep ocean dynamics to Pliocene boundary conditions that are not captured in even relatively long transient simulations (*11, 23, 38–40*). In this way, our results support the view that in some regions, subtropical drying may be a transient feature of warming rather than a stable feature of equilibrium warm climate states (*41, 42*)

In fact, observational data suggests that mechanisms of Pliocene monsoon change have direct parallels for understanding NAM variability in a warming world. Since the mid-20th century, the northeast Pacific has experienced multi-season or multi-year marine heat waves (MHW) (*43–45*). The peak of a heat wave between 2012 and 2014 occurred in summer 2014 and featured SSTs 1-2°C warmer than average on the southern California Margin (*43*), in a similar location to the region where proxies suggest the warmest mid-Pliocene temperatures occurred (Figure 5). These warmer temperatures favored higher evaporation and sensible heat fluxes from the ocean surface, increasing low level moist entropy and enhancing moist convection (Figure 5). Statistically significant rainfall changes occur in the core NAM domain, but also in peripheral regions like southern Baja California, which normally experiences atmospheric subsidence and receives little monsoon rain (Figure S6) (*19*). This is illustrated by a shift in daily summertime outgoing longwave radiation (OLR) values over southern Baja, which shows

8

an increase in values near 240-250 W/m^2. These values are characteristic of monsoon storms, while outlying low values represent tropical storms and hurricanes (Figure 5).

Warmer coastal temperatures in the 2014 MHW favored enhanced and spatially expanded NAM convection. Disentangling causality in a short instrumental record is challenging, and the cause of MHW-related SST anomalies, which result from changes in surface radiation, may differ from the cause of the California margin warming in the Pliocene, which could also involve ocean dynamical adjustments (*23, 39, 40, 43*). Despite this, there are clear parallels between our conceptual model of Pliocene NAM changes and MHW-related NAM changes; both are strongly linked to warm SSTs along the California margin. This is further corroborated by previous research showing that extreme rainfall and flooding in southern Arizona is linked to increased precipitable water offshore of Baja, similar to what we observe during the MHW (*46*). Moreover, previous work found that other NE Pacific marine heat waves are associated with above average soil moisture across the NAM domain (*47*). These extreme events in turn have important societal and ecological consequences (*36, 48, 49*).

Conclusions

SWNA is in the midst of an intensifying megadrought, driven in part by higher temperatures that increase evaporation and reduce snowpack (*50*). However, our results suggest that future hydroclimate changes may also include intervals of more intense and spatially expanded monsoon rainfall, especially if, as predicted, MHWs become more frequent in the future. While the direct influence of CO_2 is predicted to intensify individual monsoon storms (*36, 49*), coastal SST patterns complement this mechanism by facilitating the spatial expansion of monsoon rainfall into regions like Baja and Southern California. The strong linkage between coastal temperatures and NAM strength is supported by Pliocene proxies, model simulations, and our analysis of a modern MHW (Figure 5). In these settings, enhanced summer rainfall, coupled with a warming

climate, may be linked to higher fuel loads and fire, as well as flash flooding (*46, 51*). Multi-proxy studies of the Pliocene may be especially helpful for clarifying the relationships between fire, flooding, and monsoon rainfall in a warmer world.

Our results provide a new view of Pliocene SWNA hydroclimate. Instead of solely resulting from winter rain, wet conditions were at least in part driven by the summer monsoon. A warmer coastal upwelling zone drove more intense and spatially extensive summer convection, potentially resulting in intensified flooding and run off. Several modeling studies have shown that upwelling zones are especially sensitive to greenhouse boundary conditions, (*52, 53*), and it is likely that other greenhouse climate intervals witnessed similar hydroclimate reorganizations, especially near ocean upwelling zones. This mechanism is relevant to the present day, since we found evidence of an expanded monsoon during the modern 2014 marine heat wave. These results underscore the fact that far from representing a climate state fundamentally dissimilar from present day, the Pliocene can serve as an analog for the dynamical processes driving hydroclimate variability in a warm world. Further studies of the Pliocene and similar greenhouse intervals could therefore provide key lessons relevant for adapting to both near-future and long-term regional hydroclimate changes.

Materials and Methods

Site Background and Age Model

DSDP 475 (23.03°N, 109.03°W) is located within the Gulf of California near the southeastern edge of the peninsula of Baja California (Figure 1). Today, the site sits on a passive continental margin at a water depth of 2631 meters (*54*). This region of Baja California experiences northwesterly wind stress in winter and spring, although winds weaken in summer (*55*) during which time the region around DSDP 475 is primarily influenced by northward advection of waters from the eastern Pacific warm pool (*55, 56*). The Plio-Pleistocene portion of the core from DSDP

475 is predominantly composed of hemipelagic muds, transitioning to diatomaceous muds in the mid- to early-Pliocene section, showing evidence of a consistent marine setting for this site from the Pleistocene through the early Pliocene (*54*). Age control for this site's sedimentary record primarily comes from biostratigraphic tiepoints, provided in Table S2. Sedimentation rates for DSDP 475 vary between 4.4 cm/ka in the mid- to late-Pliocene (e.g. after 3.2 Ma), 3.4 cm/ka in the early Pleistocene, and then 4.1 cm/ka in the late Pleistocene (*57*). Average age uncertainty is approximately 10 kyr at each depth. Detailed age model information is provided in (*23*).

Leaf Wax Extraction and Measurement

Approximately 100 samples were processed from DSDP 475, so that the average time interval between samples was 40 kyr. After freeze drying and homogenizing sediments, total lipids were extracted using an accelerated solvent extractor system (ASE 350, Dionex) at a temperature of $100°C$ and a maximum pressure of 1500 psi. The total lipid extract (TLE) was then evaporated under a steady stream of N_2 gas. We focused our analyses on the C_{30} fatty acid, since alkanoic acids provided cleaner chromatographic traces, and wax compounds of this chain length almost exclusively derive from terrestrial plants (*16*). Fatty acids were separated from other lipid compounds on a LC-NH_2 gel column, which separates neutral and acid fractions by binding the carboxyl functional group of alkanoic acids. The neutral fraction was eluted using a 2:1 mix of dichloromethane:isopropanol, and the acid fraction was eluted with 4% acetic acid in dichloromethane. We methylated the acids to replace exchangeable hydrogen on the carboxyl group with a methyl group of known isotopic composition. The resultant FAMEs (fatty acid methyl esters) were purified again over silica gel using dichloromethane.

Concentrations of C_{30} FAMEs were determined using a GC-FID system. Hydrogen and carbon isotopic composition of the FAMEs were measured via gas chromatography-pyrolysis-

11

isotope ratio mass spectrometry (GC-IR-MS) using a Thermo Delta V Plus mass spectrometer. H_2 and CO_2 gases calibrated to an *n*-alkane standard (A7 mix provided by Arndt Schimmelmann at Indiana University) provided references for each analysis, and a synthetic mix of FAMEs was analyzed every 5-7 samples to monitor drift and correct for offsets. Samples were run in triplicate for δD to obtain a precision better than 2‰, and in duplicate or triplicate for $\delta^{13}C$ to obtain a precision better than 0.2‰. To account for the added methyl group during methylation, the δD and $\delta^{13}C$ of the methanol was determined by methylating a phthalic acid standard of known isotopic composition obtained from Arndt Schimmelmann at Indiana University, and a mass balance correction was applied to the δD and $\delta^{13}C$ values of our FAMEs. Measurements of δD were corrected for ice volume changes using a million-year smoothed version of the benthic oxygen isotope stack ((*58*)) following the method of (*59*), though this correction has a extremely small influence on the overall trend in the record (Figure S1).

Modern Plant Sampling and Inferring δD of Precipitation

Ecosystems in southern Baja California feature a transition zone between Sonoran desert vegetation and Cape region vegetation, otherwise known as thornscrub vegetation. The region features high floristic diversity, with cacti and small trees forming a dense understory. Common tree species belong to the legume family and include *Cercidium peninsulare*, *Cassia atomaria*, and *Lysiloma microphylla* (*60*). We suggest that site 475 receives aeolian wax inputs from this region, as well as from Sonoran desert vegetation to the east of the Gulf of California in the Mexican states of Sonora and Sinaloa. We therefore use measurements of modern leaf waxes from both thornscrub and Sonoran desert vegetation to evaluate the controls on leaf wax isotopes and improve interpretations of our record.

δD_{wax} values are offset from the hydrogen isotopic signature of the water from which they are

synthesized (assumed to be the isotopic value of mean annual precipitation or δD_p). This value is known as the apparent fractionation, or ε_{p-w}. Values of ε are related to ecological differences in wax synthesis across plant clades. Robust evidence suggests that waxes synthesized by graminoids tend to have a larger ε_{p-w}, or are more depleted relative to δD_p, than eudicots (e.g. broadleaved herbs, shrubs and trees (*16*)). These differences are likely the result of systematic differences in the seasonal leaf wax production in each group, or differences in the pools of intermediate hydrocarbon compounds used in leaf wax synthesis (*61*). Members of Cactaceae, which use the Crassulaic Acid Metabolism (CAM photosynthesis), are also present in the Sonoran Desert. Greenhouse experiments suggest that CAM species may have similar ε values to eudicots (*61*). However, we suggest that members of Cactaceae may not be major contributors to sedimentary leaf waxes, and that the majority of input comes from C_3 eudicots and C_4 monocots. Herbs and shrubs in the NAM region primarily using the C_3 pathway, while most grasses are C_4 taxa (*16*). C_3 and C_4 taxa exhibit differences in leaf wax $\delta^{13}C$, with a more enriched carbon isotopic signature in C_4 graminoids.

We therefore use paired measurements of carbon and hydrogen isotopes in leaf waxes to identify the proportion of leaf waxes that come from C_4 graminoids in contrast to eudicots, and then apply appropriate ε_{p-w} offsets to obtain δD_p values from wax isotopic data. This mass balance approach is widely used in the literature, and represents ε_{p-w} values as a function of the proportion of the fraction of C_4 and C_3 taxa in a given sample of sedimentary leaf waxes (Eq. 1). This ε value is then used to adjust δD_{wax} values to obtain δD_p (Eq. 2).

$$\varepsilon = f_{C4} \cdot \varepsilon_{C4} + (1 - f_{C4}) \cdot \varepsilon_{C3} \tag{1}$$

$$\delta D_{precip} = \frac{1000 + \delta D_{wax}}{(\varepsilon/1000) + 1} - 1000 \tag{2}$$

End-members of δ^{13}C values were obtained from our own measurements of alkanes and alkanoic acids from the modern plant communities at the Arizona-Sonora Desert Museum, which include taxa from both the Sonoran Desert ecoregion and southern Baja Thornscrub vegetation (Table S3). These values are based on repeated measurement of new growth on each plant once a month for a calendar year. In order to make measurements more comparable to Plio-Pleistocene leaf wax carbon isotopes measurements, values of δ^{13}C inferred from modern plants have been corrected for the Suess effect. Estimates of ε_{p-w} for C$_4$ and C$_3$ taxa were obtained by comparing measures of δD_{wax} for the C$_{29}$ n-alkane to amount-weighted annual average δD_p ($-52.2\,$‰) from the Tucson GNIP station (*62*). While the majority of our measurements come from the C$_{29}$ n-alkane, we find no evidence of an offset between ε_{p-w} values estimated for alkanes vs. alkanoic acids, which coheres with the results of previous work (*16, 61*). Because our dataset has few measurements of C$_4$ graminoids, we augment our compilation with published estimates of ε_{p-w} from the western US (*63, 64*). However, we note that these data largely agree with our estimates of ε from the Desert Museum dataset, and end-member estimates of ε and δ^{13}C would be nearly identical if relying exclusively on the Desert Museum dataset.

Our mass balance correction to obtain δD_p is performed within a Bayesian framework, similar to the formulation used by (*17, 65*). Briefly, we calculate the proportion of C$_4$ taxa in a given sample (f_{C4}) by estimating the probability that a given down-core carbon isotope measurement is more likely to be drawn from a C$_4$ or C$_3$ plant community. Because of variability among different C$_4$ and C$_3$ plants' δ^{13}C values, we model carbon isotopic values as normal distributions with mean and standard deviation using the data in Table S3. These estimates are then used to create an ensemble of ε values to be applied to raw δD_{wax} measurements in order to generate a robust, error-propagated estimate of δD_p. Details of calculations are provided in (*17*).

Climatology and Interpretation of Inferred δD of Precipitation

Plio-Pleistocene changes in leaf wax isotopes reflect changes in the intensity and spatial extent of moist convection over the core NAM region and Baja California. Modern core-top samples show a more enriched value of inferred δD_p in the southern Gulf of California, where monsoon rainfall contributes a greater proportion of annual precipitation (Figure S2). Previous work has shown a strong positive correlation between values of δD_p inferred from leaf waxes and the importance of monsoon convection in the annual cycle of precipitation (e.g. % changes in NAM convection) (*17*).

Monsoon convection exhibits more positive values of δD_p than non-monsoonal (e.g. wintertime) rainfall. Monsoon rainfall is characterized by deep convection during the summer months. Currently, in the NAM region, the spatial pattern of % monsoon rainfall is strongly correlated with the spatial pattern in monthly outgoing longwave radiation (OLR), a proxy for deep convection whereby lower values represent colder cloud tops (r = -0.85) (*66*). Deep convective monsoon rainfall result from ice hydrometeors that develop when vapor evaporated in a warm, saturated boundary layer is lifted in strong updrafts, resulting in a more enriched isotopic signature for rainfall (*18*). In contrast, stratiform rainfall tends to form in environments with relatively weak updrafts, and may develop relatively slowly, incorporating mid to upper tropospheric water vapor and undergoing more phase changes, resulting in a depleted isotopic signature (*18*). Winter storms that originate in distant locations also have a more depleted signature compared to summer as a result of Rayleigh distillation processes. We therefore expect intervals with enhanced deep convective and monsoon rainfall to exhibit more enriched values of δD_p, since a greater proportion of annual rainfall comes from enriched, convective rainfall. In contrast, we expect intervals with a weaker monsoon and less deep convection, as well as more winter rainfall will likely exhibit more negative values δD_p. This is opposite to the 'amount effect,' where more rainfall is associated with a more depleted isotopic signature (*67*), but is

15

consistent with our understanding of regional isotope systematics.The NAM region differs from other tropical regions (e.g. the Asian monsoon) as it receives a substantial amount of stratiform rainfall, which likely overprints any 'amount effect (*68*).

Other processes, like temperature and changes in vapor source region, may influence inferred δD_p values. Equilibrium temperature effects (e.g. changes in the fractionation between atmospheric water vapor and rainfall) likely only account for 20-30% of the overall change observed in δD_p values at most. SST anomalies between 3.5 and 3.0 Ma at DSDP 475 were between 4-6°C warmer than pre-industrial values (*23*), which would translate into a 4 to 6 ‰ change in δD_p relative to atmospheric water vapor, assuming that condensation temperatures shifted similarly to SSTs (*23*). This calculation does not account for changes in kinetic effects, or in changes in vapor source region. To analyze the potential impact of these factors on the record from DSDP 475, we analyze isotope enabled simulations of the Community Earth System Model, version 1.2 (iCESM1.2).

SST Compilation

To identify relationships between leaf wax-inferred δD_p and Plio-Pleistocene changes in large-scale circulation over the north Pacific, we compiled alkenone-based continuous reconstructions of Plio-Pleistocene temperatures from the northeast Pacific, and interpolated them to a common timestep (e.g. 0.05 Ma or 50 ka between adjacent values) (*22–24, 69–79*). Records were calibrated using `BAYSPLINE`, a Bayesian calibration that accounts for the attenuation of the relationship between the alkenone unsaturation index and temperature at warmer temperatures (*80*). Analytical and calibration errors were propagated through the full suite of δD_p and calibrated SST values. We then calculated correlations between δD_p and SSTs using the full suite of uncertainty in each record, excluding records that only provide timeslice estimates of mid-Pliocene temperatures, or have extremely low resolution for the interval of interest (e.g.

16

sites 1018 and 1338). Site 475 δD_p shows a robust positive correlation SST records on the southern California margin (e.g. greater than 0.5), and is also positively associated with SSTs in the eastern equatorial Pacific (Figure S4). The site is negative correlated with north Pacific temperature records at sites 882 and 1417 (Figure S4). Our southern California Margin SST index (shown in Figure 2) is calculated by taking the first EOF of records from sites 1014,1012, 1010, and 475. This mode explains 83% of the variance across these sites (Figure S4), and loads most strongly onto 475, 1012, and 1014.

Reduced Space Reconstruction

One of the iCAM5 simulations uses an alkenone SST proxy-based reduced space reconstruction of mid-Pliocene Pacific SST anomalies relative to preindustrial. This is an updated version of the reconstruction presented in (*11*). The approach is identical to the method described in (*11*), except, 1) the COBE SST product (*81*) is used to derive modern Pacific EOFs instead of ERSSTv5, 2) additional SST records that were published in recent years have been added, and 3) we widened the target interval for the mid-Pliocene to 5–3 Ma, rather than focusing solely on the mid-Piacenzian time (3.3–3 Ma). ref. (*11*) focused on the Piacenzian in order to compare the reconstruction with PlioMIP simulations; here, we are more interested in testing the response of the atmosphere to the warm California current (and more broadly, the Pliocene SST pattern). Widening the time window allows for more data points to be included for lower resolution records, and recognizes that in some locations peak warmth occurred earlier than 3.3 Ma. Supplementary Table 1 lists the sites used. The reconstruction is similar to the original result in (*11*) (Figure S7).

Isotope-Enabled Model Simulations

To investigate the drivers of SWNA δD_p changes during the Pliocene, we analyzed monsoon changes in a simulation of isotopologue-tracking enabled CESM1.2 (iCESM1.2) in atmosphere-only mode (e.g. iCAM5) (82). Simulations are run at a 0.9°x1.25° horizontal resolution, with 30 vertical layers. The pre-industrial simulation of iCESM1.2 used in this study captures a similar seasonal cycle of water vapor isotopes compared to GNIP observations, with an enriched summer monsoon compared to depleted winter rainfall (Figure S6), despite the fact that iCESM1.2's rainfall isotopes are depleted compared to observations at Tucson's GNIP station (83). In addition, while many isotope enabled models struggle to reproduce the negative correlation between the stratiform rainfall fraction and rainfall isotopes seen in observational data, iCAM5 performs slightly better than other models at simulating rainfall isotope changes due to changing stratiform fraction (29).

One simulation used a bias-corrected Pacific mid-Pliocene SST field. A key benefit of this approach is that fully coupled Pliocene simulations that feature altered Pliocene topography and land surface conditions struggle to produce the magnitude of SST anomalies suggested by proxy data on the California margin, limiting their utility for studying the relationship between Pliocene SSTs and hydroclimate in this region (23). The reconstructed SSTs by the reduced space reconstruction (Figure S7b) were used in the region from 165°E - 60°W and 40°S - 60°N to correct simulated Pliocene SSTs by CESM1.2 (38). In this region, reconstructed Pliocene anomalies from the reduced space field were added to pre-industrial SSTs simulated by the model. Outside this region, SSTs were held to values obtained from a coupled mid-Pliocene simulation of CESM1.2 (38). All other boundary conditions are kept at preindustrial levels, although CO_2 was increased to Pliocene levels, at 400 ppm. Since the direct influence of CO_2 is known to stabilize the atmosphere (26), this simulation allows us to explore whether warm coastal SSTs, even in the presence of higher CO_2, can result in a stronger monsoon.

We also analyzed a simulation with idealized SSTs to help link spatial patterns of SST to SWNA precipitation and δD_p. These used SSTs from (*15*), which uses the PRISM3 SST reconstruction (*28*), but increases temperatures on the Southern California Margin to match proxy evidence. All other boundary conditions (e.g. topography, land surface conditions), including CO_2, are kept at pre-industrial values. This simplified experimental design allows us to cleanly isolate the influence of an altered SST field on SW NA hydroclimate.

Marine Heat Wave Analysis

We analyze atmospheric changes associated with the 2013-2014 marine heat wave over Baja California and the core monsoon domain. SST anomalies off the coast of Baja reached their maximum in summer 2014 (*43*). We obtain SST anomalies from (*81*), and use reanalysis data from the North American Regional Reanalysis (NARR) (*84*) to plot changes in precipitation and calculate changes in equivalent potential temperature θ_e. Finally, to further quantify changes in deep convection associated with the 2013-2014 marine heat wave (MHW) described in the main text, we plot changes in summertime (June - September) climatological outgoing longwave radiation (OLR) over southern Baja California as well as the distribution of OLR values during the heat wave (*66*). Lower values of OLR indicate cooler cloud tops and deeper convection 2013-2014 values are more strongly left-skewed than the climatology (Figure 5). While some extremely low values near 200 W/m² are the result of hurricanes (e.g. hurricane Odile in 2014), more moderate values near 225-240 W/m² represent deep convection from monsoon storms (*85*), and still fall outside the climatological 95% confidence interval values of OLR. This suggests that increases in rainfall during the MHW are the result of increases in monsoon rainfall and not just the result of tropical storms and hurricanes.

References

1. M. Pound, *et al.*, Late Pliocene lakes and soils: a global data set for the analysis of climate feedbacks in a warmer world. *Climate of the Past* **10**, 167–180 (2014).

2. D. E. Ibarra, *et al.*, Warm and cold wet states in the western United States during the Pliocene–Pleistocene. *Geology* **46**, 355–358 (2018).

3. P. Remeika, I. W. Fischbein, S. A. Fischbein, Lower Pliocene petrified wood from the Palm Spring Formation, Anza Borrego Desert State Park, California. *Review of palaeobotany and palynology* **56**, 183–198 (1988).

4. R. A. Ballog, R. E. Malloy, *Neogene Palynology from the Southern California Continental Borderland, Site 467, Deep Sea Drilling Project Leg 64*, vol. 63 of *Initial Reports of the Deep Sea Drilling Project, 63* (U.S. Government Printing Office, 1981).

5. U. Salzmann, A. M. Haywood, D. J. Lunt, The past is a guide to the future? Comparing Middle Pliocene vegetation with predicted biome distributions for the twenty-first century. *Philosophical Transactions of the Royal Society A: Mathematical, Physical and Engineering Sciences* **367**, 189–204 (2009).

6. W. E. Miller, The late Pliocene Las Tunas local fauna from southernmost Baja California, Mexico. *Journal of Paleontology* pp. 762–805 (1980).

7. M. P. Byrne, P. A. O'Gorman, The response of precipitation minus evapotranspiration to climate warming: Why the "wet-get-wetter, dry-get-drier" scaling does not hold over land. *Journal of Climate* **28**, 8078–8092 (2015).

8. R. Seager, N. Naik, G. A. Vecchi, Thermodynamic and dynamic mechanisms for large-scale changes in the hydrological cycle in response to global warming. *Journal of climate* **23**, 4651–4668 (2010).

9. N. J. Burls, A. V. Fedorov, Wetter subtropics in a warmer world: Contrasting past and future hydrological cycles. *Proceedings of the National Academy of Sciences* **114**, 12888–12893 (2017).

10. A. V. Fedorov, N. J. Burls, K. T. Lawrence, L. C. Peterson, Tightly linked zonal and meridional sea surface temperature gradients over the past five million years. *Nature Geoscience* **8**, 975–980 (2015).

11. J. E. Tierney, A. M. Haywood, R. Feng, T. Bhattacharya, B. L. Otto-Bliesner, Pliocene warmth consistent with greenhouse gas forcing. *Geophysical Research Letters* **46**, 9136–9144 (2019).

12. P. Molnar, M. A. Cane, El Niño's tropical climate and teleconnections as a blueprint for pre-Ice Age climates. *Paleoceanography* **17**, 11–1 (2002).

13. D. I. Axelrod, Climate and evolution in western North America during middle Pliocene time. *Evolution* pp. 127–144 (1948).

14. B. I. Cook, R. Seager, The response of the North American Monsoon to increased greenhouse gas forcing. *Journal of Geophysical Research: Atmospheres* **118**, 1690–1699 (2013).

15. M. Fu, M. A. Cane, P. Molnar, E. Tziperman, Warmer Pliocene upwelling site SST leads to wetter subtropical coastal areas: a positive feedback on SST. *Paleoceanography and Paleoclimatology* p. e2021PA004357 (2022).

16. D. Sachse, *et al.*, Molecular paleohydrology: interpreting the hydrogen-isotopic composition of lipid biomarkers from photosynthesizing organisms. *Annual Review of Earth and Planetary Sciences* **40**, 221–249 (2012).

17. T. Bhattacharya, J. E. Tierney, J. A. Addison, J. W. Murray, Ice-sheet modulation of deglacial North American monsoon intensification. *Nature Geoscience* **11**, 848–852 (2018).

18. P. K. Aggarwal, *et al.*, Proportions of convective and stratiform precipitation revealed in water isotope ratios. *Nature Geoscience* **9**, 624–629 (2016).

19. M. Fonseca-Hernandez, C. Turrent, Y. G. Mayor, I. Tereshchenko, Using observational and reanalysis data to explore the southern Gulf of California boundary layer during the North American Monsoon onset. *Journal of Geophysical Research: Atmospheres* **126**, e2020JD033508 (2021).

20. M. J. Pound, A. M. Haywood, U. Salzmann, J. B. Riding, Global vegetation dynamics and latitudinal temperature gradients during the mid to late miocene (15.97–5.33 ma). *Earth-Science Reviews* **112**, 1–22 (2012).

21. C. M. Brierley, *et al.*, Greatly expanded tropical warm pool and weakened Hadley circulation in the early Pliocene. *Science* **323**, 1714–1718 (2009).

22. P. S. Dekens, A. C. Ravelo, M. D. McCarthy, Warm upwelling regions in the Pliocene warm period. *Paleoceanography* **22** (2007). _eprint: https://onlinelibrary.wiley.com/doi/pdf/10.1029/2006PA001394.

23. P. R. Brennan, T. Bhattacharya, R. Feng, J. E. Tierney, E. Jorgensen, Low cloud changes govern northeast Pacific response to Pliocene boundary conditions. *Paleoceanography and Paleoclimatology* (in review).

24. J. P. LaRiviere, *et al.*, Late Miocene decoupling of oceanic warmth and atmospheric carbon dioxide forcing. *Nature* **486**, 97–100 (2012). Number: 7401 Publisher: Nature Publishing Group.

25. S.-P. Xie, *et al.*, Global warming pattern formation: Sea surface temperature and rainfall. *Journal of Climate* **23**, 966–986 (2010).

26. S. Pascale, *et al.*, Weakening of the North American monsoon with global warming. *Nature Climate Change* **7**, 806–812 (2017).

27. J. T. Abell, G. Winckler, R. F. Anderson, T. D. Herbert, Poleward and weakened westerlies during Pliocene warmth. *Nature* **589**, 70–75 (2021).

28. H. Dowsett, M. Robinson, K. Foley, Pliocene three-dimensional global ocean temperature reconstruction. *Climate of the Past* **5**, 769–783 (2009).

29. J. Hu, J. Emile-Geay, J. Nusbaumer, D. Noone, Impact of convective activity on precipitation δ 18o in isotope-enabled general circulation models. *Journal of Geophysical Research: Atmospheres* **123**, 13–595 (2018).

30. B. I. Cook, T. R. Ault, J. E. Smerdon, Unprecedented 21st century drought risk in the American Southwest and Central Plains. *Science Advances* **1**, e1400082 (2015).

31. Y. Zhu, R.-H. Zhang, J. Sun, North Pacific Upper-Ocean Cold Temperature Biases in CMIP6 Simulations and the Role of Regional Vertical Mixing. *Journal of Climate* **33**, 7523–7538 (2020).

32. E. D. Maloney, *et al.*, North American climate in CMIP5 experiments: Part III: Assessment of twenty-first-century projections. *Journal of Climate* **27**, 2230–2270 (2014).

33. J. D. Meyer, J. Jin, The response of future projections of the North American monsoon when combining dynamical downscaling and bias correction of CCSM4 output. *Climate Dynamics* **49**, 433–447 (2017).

34. M. Almazroui, *et al.*, Projected changes in temperature and precipitation over the United States, Central America, and the Caribbean in CMIP6 GCMs. *Earth Systems and Environment* **5**, 1–24 (2021).

35. S. Moon, K.-J. Ha, Future changes in monsoon duration and precipitation using CMIP6. *npj Climate and Atmospheric Science* **3**, 1–7 (2020).

36. S. Pascale, S. B. Kapnick, S. Bordoni, T. L. Delworth, The influence of CO2 forcing on North American monsoon moisture surges. *Journal of Climate* **31**, 7949–7968 (2018).

37. C. He, T. Li, W. Zhou, Drier North American monsoon in contrast to Asian–African monsoon under global warming. *Journal of Climate* **33**, 9801–9816 (2020).

38. R. Feng, B. L. Otto-Bliesner, E. C. Brady, N. Rosenbloom, Increased climate response and earth system sensitivity from CCSM4 to CESM2 in mid-Pliocene simulations. *Journal of Advances in Modeling Earth Systems* **12**, e2019MS002033 (2020).

39. A. Fedorov, *et al.*, Patterns and mechanisms of early Pliocene warmth. *Nature* **496**, 43–49 (2013).

40. H. L. Ford, A. C. Ravelo, P. S. Dekens, J. P. LaRiviere, M. W. Wara, The evolution of the equatorial thermocline and the early Pliocene El Padre mean state. *Geophysical Research Letters* **42**, 4878–4887 (2015).

41. J. Sniderman, *et al.*, Southern Hemisphere subtropical drying as a transient response to warming. *Nature Climate Change* **9**, 232–236 (2019).

42. G. Zappa, P. Ceppi, T. G. Shepherd, Time-evolving sea-surface warming patterns modulate the climate change response of subtropical precipitation over land. *Proceedings of the National Academy of Sciences* **117**, 4539–4545 (2020).

43. T. A. Myers, C. R. Mechoso, G. V. Cesana, M. J. DeFlorio, D. E. Waliser, Cloud feedback key to marine heatwave off Baja California. *Geophysical Research Letters* **45**, 4345–4352 (2018).

44. D. J. Amaya, A. J. Miller, S.-P. Xie, Y. Kosaka, Physical drivers of the summer 2019 North Pacific marine heatwave. *Nature communications* **11**, 1–9 (2020).

45. O. Hoegh-Guldberg, *et al.*, *The Ocean. In: Climate Change 2014: Impacts, Adaptation, and Vulnerability. Part B: Regional Aspects. Contribution of Working Group II to the Fifth Assessment Report of the Intergovernmental Panel on Climate Change* (Intergovernmental Panel on Climate Change, 2014).

46. L. Yang, J. Smith, M. L. Baeck, E. Morin, D. C. Goodrich, Flash flooding in arid/semiarid regions: Dissecting the hydrometeorology and hydrology of the 19 August 2014 storm and flood hydroclimatology in Arizona. *Journal of Hydrometeorology* **18**, 3103–3123 (2017).

47. H. Shi, *et al.*, Co-occurrence of california drought and northeast pacific marine heatwaves under climate change. *Geophysical Research Letters* **48**, e2021GL092765 (2021).

48. J. J. Mazon, *et al.*, Objective climatological analysis of extreme weather events in Arizona during the North American monsoon. *Journal of Applied Meteorology and Climatology* **55**, 2431–2450 (2016).

49. E. M. Demaria, *et al.*, Intensification of the North American Monsoon rainfall as observed from a long-term high-density gauge network. *Geophysical Research Letters* **46**, 6839–6847 (2019).

50. A. P. Williams, B. I. Cook, J. E. Smerdon, Rapid intensification of the emerging southwestern North American megadrought in 2020–2021. *Nature Climate Change* pp. 1–3 (2022).

51. K. A. Moloney, *et al.*, Increased fire risk in Mojave and Sonoran shrublands due to exotic species and extreme rainfall events. *Ecosphere* **10**, e02592 (2019).

52. T. Schneider, C. M. Kaul, K. G. Pressel, Possible climate transitions from breakup of stratocumulus decks under greenhouse warming. *Nature Geoscience* **12**, 163–167 (2019).

53. J. Zhu, C. J. Poulsen, J. E. Tierney, Simulation of Eocene extreme warmth and high climate sensitivity through cloud feedbacks. *Science advances* **5**, eaax1874 (2019).

54. J. Curray, *et al.*, *Baja California Passive Margin Transect: Sites 474, 475, and 476*, vol. 64 of *Initial Reports of the Deep Sea Drilling Project, 64* (U.S. Government Printing Office, 1982).

55. O. Zaytsev, R. Cervantes-Duarte, O. Montante, A. Gallegos-Garcia, Coastal upwelling activity on the Pacific shelf of the Baja California Peninsula. *Journal of oceanography* **59**, 489–502 (2003).

56. R. Durazo, T. Baumgartner, Evolution of oceanographic conditions off Baja California: 1997–1999. *Progress in Oceanography* **54**, 7–31 (2002).

57. M.-P. Aubry, *Calcareous nannofossil biostratigraphy, Leg 64.*, vol. 64 of *Initial Reports of the Deep Sea Drilling Project, 64* (U.S. Government Printing Office, 1982).

58. L. E. Lisiecki, M. E. Raymo, A Pliocene-Pleistocene stack of 57 globally distributed benthic δ18O records. *Paleoceanography* **20** (2005).

59. D. P. Schrag, G. Hampt, D. W. Murray, Pore fluid constraints on the temperature and oxygen isotopic composition of the glacial ocean. *Science* **272**, 1930–1932 (1996).

60. F. Shreve, The vegetation of the cape region of baja california. *Madroño* **4**, 105–113 (1937).

61. L. Gao, E. J. Edwards, Y. Zeng, Y. Huang, Major evolutionary trends in hydrogen isotope fractionation of vascular plant leaf waxes. *PloS one* **9**, e112610 (2014).

62. C. Eastoe, D. Dettman, Isotope amount effects in hydrologic and climate reconstructions of monsoon climates: Implications of some long-term data sets for precipitation. *Chemical Geology* **430**, 78–89 (2016).

63. S. J. Feakins, A. L. Sessions, Controls on the D/H ratios of plant leaf waxes in an arid ecosystem. *Geochimica et Cosmochimica Acta* **74**, 2128–2141 (2010).

64. F. A. Smith, K. H. Freeman, Influence of physiology and climate on δD of leaf wax n-alkanes from C3 and C4 grasses. *Geochimica et Cosmochimica Acta* **70**, 1172–1187 (2006).

65. J. E. Tierney, F. S. Pausata, P. B. deMenocal, Rainfall regimes of the Green Sahara. *Science advances* **3**, e1601503 (2017).

66. B. Liebmann, C. A. Smith, Description of a complete (interpolated) outgoing longwave radiation dataset. *Bulletin of the American Meteorological Society* **77**, 1275–1277 (1996).

67. C. Risi, S. Bony, F. Vimeux, Influence of convective processes on the isotopic composition (δ18O and δD) of precipitation and water vapor in the tropics: 2. Physical interpretation of the amount effect. *Journal of Geophysical Research: Atmospheres* **113** (2008).

68. C. Schumacher, R. A. Houze, The TRMM precipitation radar's view of shallow, isolated rain. *Journal of Applied Meteorology and Climatology* **42**, 1519–1524 (2003).

69. M. L. Sánchez-Montes, *et al.*, Late Pliocene Cordilleran Ice Sheet development with warm northeast Pacific sea surface temperatures. *Climate of the Past* **16**, 299–313 (2020).

70. H. Dowsett, *et al.*, The PRISM4 (mid-Piacenzian) paleoenvironmental reconstruction. *Climate of the Past* **12**, 1519–1538 (2016).

71. C. M. Brierley, *et al.*, Greatly Expanded Tropical Warm Pool and Weakened Hadley Circulation in the Early Pliocene. *Science* **323**, 1714–1718 (2009). Publisher: American Association for the Advancement of Science Section: Report.

72. J. Liu, *et al.*, Eastern equatorial Pacific cold tongue evolution since the late Miocene linked to extratropical climate. *Science Advances* **5**, eaau6060 (2019). Publisher: American Association for the Advancement of Science Section: Research Article.

73. G. Rousselle, C. Beltran, M.-A. Sicre, I. Raffi, M. De Rafélis, Changes in sea-surface conditions in the Equatorial Pacific during the middle Miocene–Pliocene as inferred from coccolith geochemistry. *Earth and Planetary Science Letters* **361**, 412–421 (2013).

74. Y. G. Zhang, M. Pagani, Z. Liu, A 12-Million-Year Temperature History of the Tropical Pacific Ocean. *Science* **344**, 84–87 (2014). Publisher: American Association for the Advancement of Science Section: Report.

75. T. D. Herbert, *et al.*, Late Miocene global cooling and the rise of modern ecosystems. *Nature Geoscience* **9**, 843–847 (2016). Number: 11 Publisher: Nature Publishing Group.

76. K. T. Lawrence, Z. Liu, T. D. Herbert, Evolution of the Eastern Tropical Pacific Through Plio-Pleistocene Glaciation. *Science* **312**, 79–83 (2006). Publisher: American Association for the Advancement of Science Section: Research Article.

77. O. Seki, *et al.*, Paleoceanographic changes in the Eastern Equatorial Pacific over the last 10 Myr. *Paleoceanography* **27** (2012). _eprint: https://agupubs.onlinelibrary.wiley.com/doi/pdf/10.1029/2011PA002158.

78. J. Etourneau, R. Schneider, T. Blanz, P. Martinez, Intensification of the Walker and Hadley atmospheric circulations during the Pliocene–Pleistocene climate transition. *Earth and Planetary Science Letters* **297**, 103–110 (2010).

79. H. b. Shaari, M. Yamamoto, T. Irino, Enhanced upwelling in the eastern equatorial Pacific at the last five glacial terminations. *Palaeogeography, Palaeoclimatology, Palaeoecology* **386**, 8–15 (2013).

80. J. E. Tierney, M. P. Tingley, BAYSPLINE: A new calibration for the alkenone paleothermometer. *Paleoceanography and Paleoclimatology* **33**, 281–301 (2018).

81. M. Ishii, A. Shouji, S. Sugimoto, T. Matsumoto, Objective analyses of sea-surface temperature and marine meteorological variables for the 20th century using icoads and the kobe collection. *International Journal of Climatology: A Journal of the Royal Meteorological Society* **25**, 865–879 (2005).

82. E. Brady, *et al.*, The connected isotopic water cycle in the Community Earth System Model version 1. *Journal of Advances in Modeling Earth Systems* **11**, 2547–2566 (2019).

83. J. Nusbaumer, T. E. Wong, C. Bardeen, D. Noone, Evaluating hydrological processes in the C ommunity A tmosphere M odel V ersion 5 (C AM5) using stable isotope ratios of water. *Journal of Advances in Modeling Earth Systems* **9**, 949–977 (2017).

84. Mesinger, Fedor and DiMego, Geoff and Kalnay, Eugenia and Mitchell, Kenneth and Shafran, Perry C and Ebisuzaki, Wesley and Jović, Dušan and Woollen, Jack and Rogers, Eric and Berbery, Ernesto H and others, North american regional reanalysis. *Bulletin of the American Meteorological Society* **87**, 343–360 (2006).

85. I. T. Okabe, The North American monsoon, Ph.D. thesis, University of British Columbia (1995).

Acknowledgements

Data Availability Statement

New proxy data, the updated reduced space reconstruction, and selected modeled fields will be archived at a permanent link at the NOAA Paleoclimatology Database and will be made available upon publication. SST Data used in reduced space reconstruction provided in a Supplementary File.

Supplementary materials

Materials and Methods

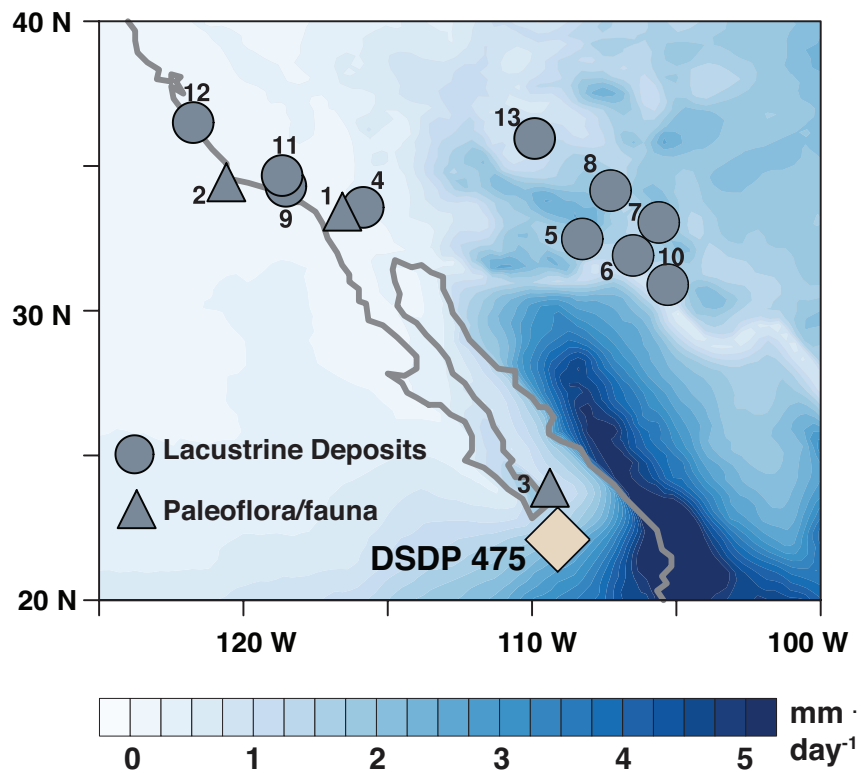Supplementary Text

Figs. S1 to S3

Tables S1 to S4

References *(4-10)*

Figure 1: **Regional changes in southwestern North America during the Pliocene.** Map shows location of previously studied sites discussed in text (Table S1) as well as location of DSDP 475. Background contours climatological monsoon (July-September) rainfall from the North American Regional Reanalysis (*84*).
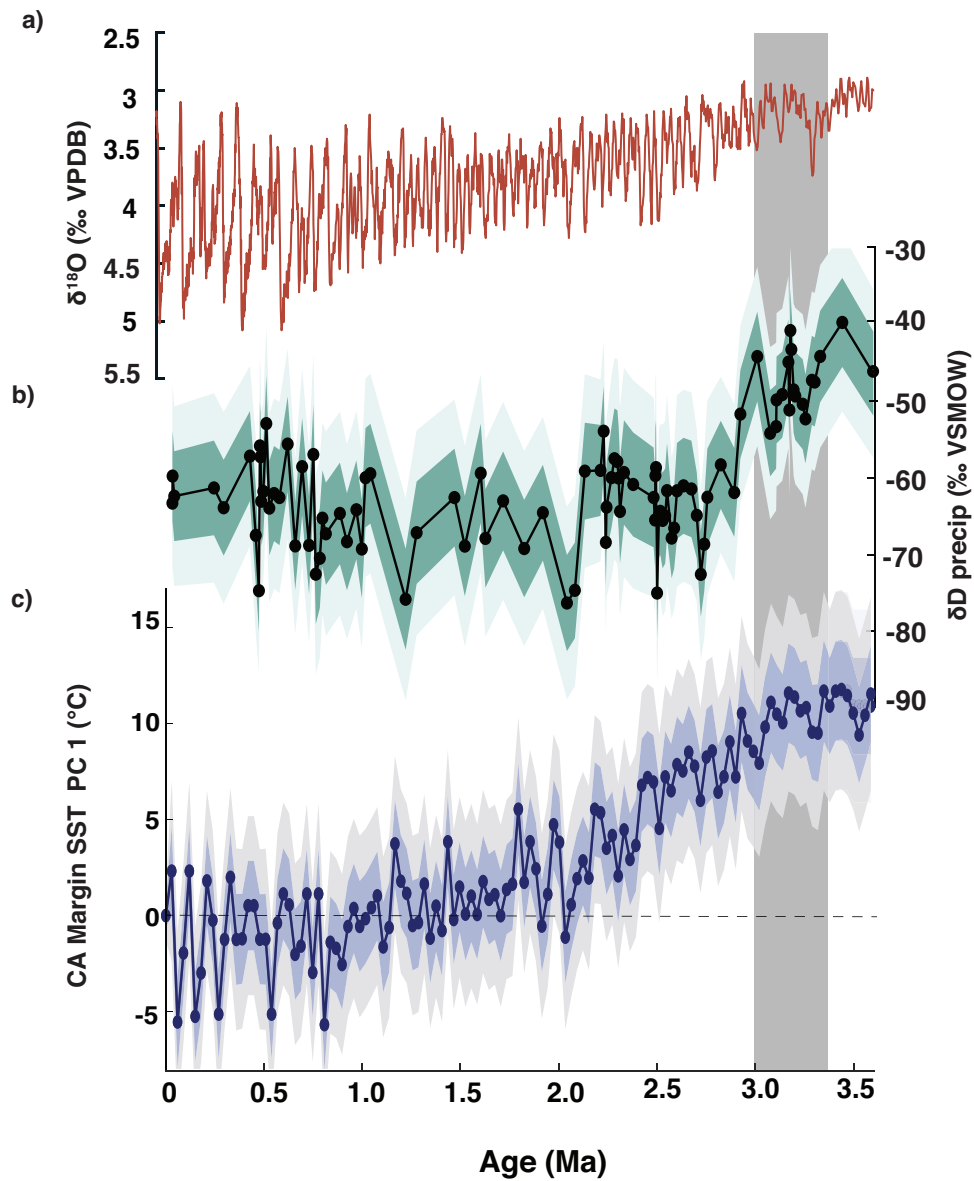
Figure 2: **Plio-Pleistocene changes in SW NA hydroclimate.** a) shows benthic oxygen isotope stack from (*58*), while b) shows our new Plio-Pleistocene reconstruction of δD_p from DSDP 475. Finally, c)shows an index of Plio-Pleistocene southern California margin temperatures (see Methods).
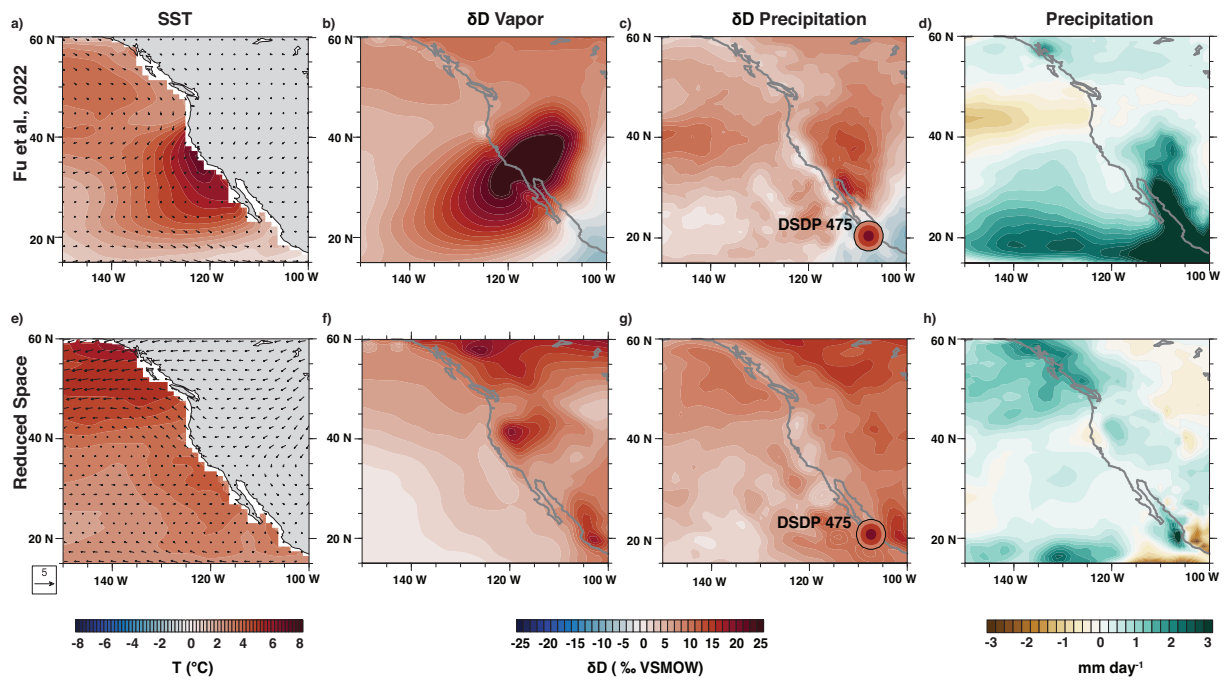
Figure 3: **Changes in summer rainfall and water isotopes in two isotope-enabled simulations.** Top row shows iCAM5 results forced with SST changes in (*15*), while bottom row shows iCAM5's response to our reduced space SST reconstruction. a,e) show June-September SST patterns with wind anomalies in each simulation. b,f) show vertically integrated δD of vapor.c,g) show δD_p; and for reference, comparison to lower (outer circle), median (middle circle), and upper (inner circle) 95% confidence interval of proxy-estimated δD_p changes at site 475. Finally, panels d) and h) show precipitation changes.
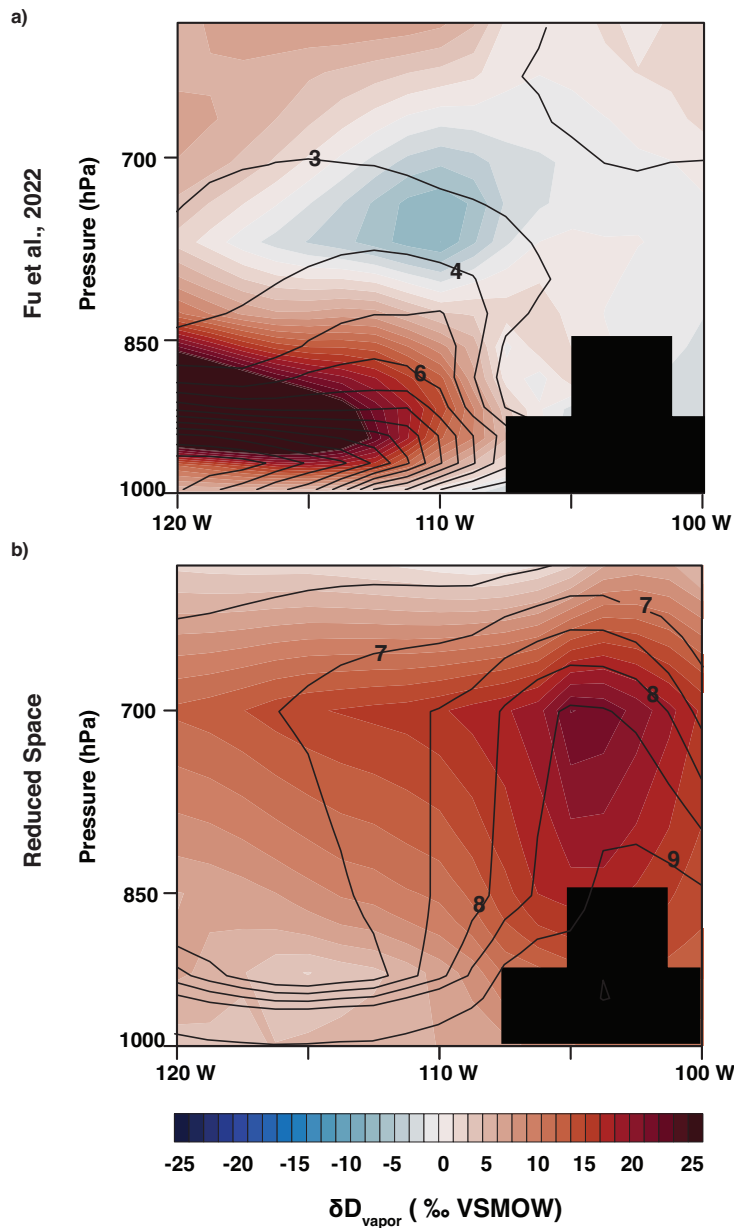
Figure 4: **Relationship between water vapor isotopes and changes in the energy available for convection.** Vertical profiles are averaged over 120-100°W and 20 - 30°N. Solid contours show anomalies of equivalent potential temperature or θ_e, while colored contours show anomalies of atmospheric water vapor δD. a) shows results for iCAM5 simulation using SSTs from (*15*), while b) shows results from new iCAM5 using reduced-space SST reconstruction.
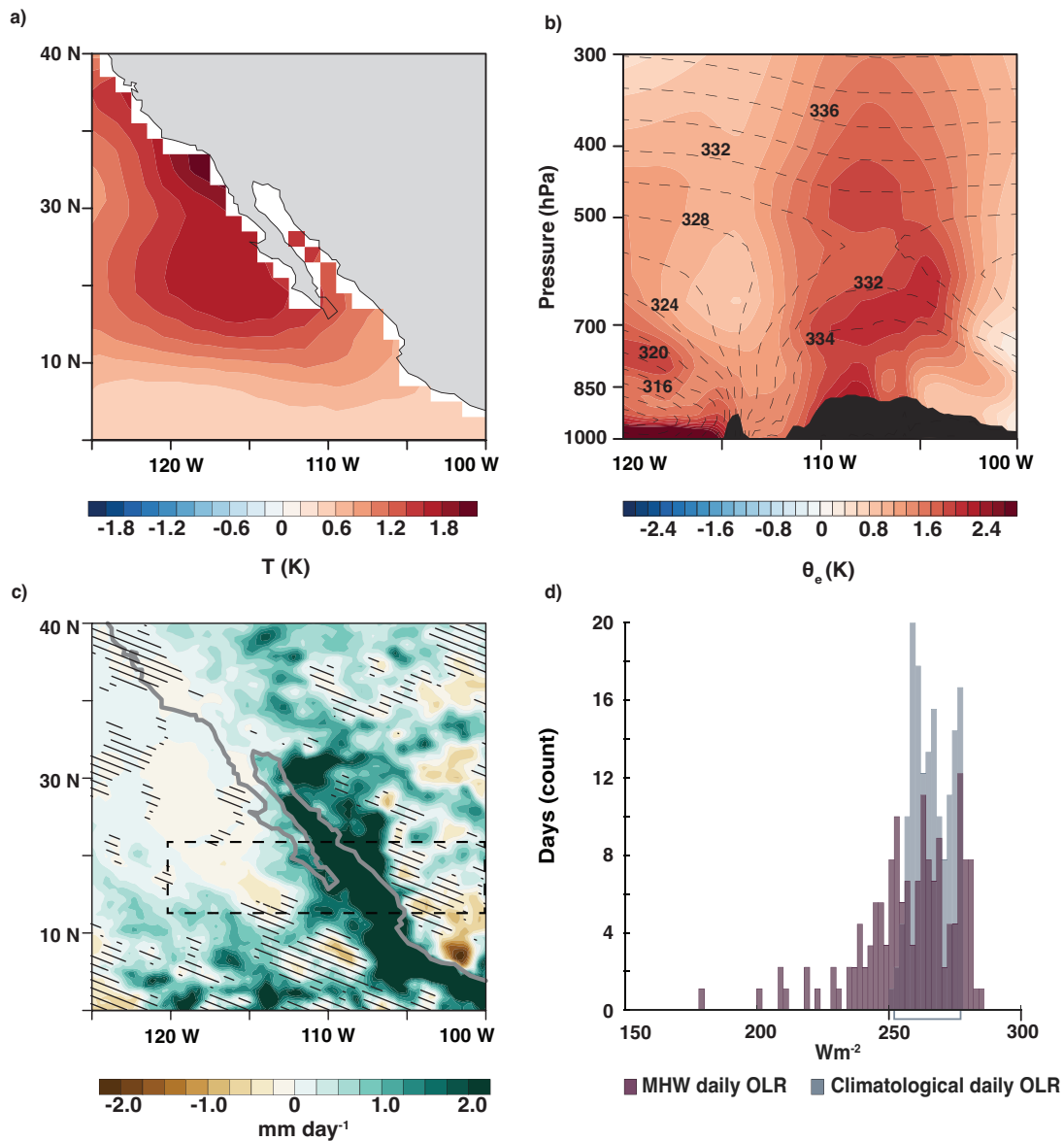
Figure 5: **NAM changes during the peak of the 2014 northeast Pacific MHW.** a) shows SST anomalies during summer 2014, during the peak of the MHW. b) vertical atmospheric profile of moist entropy changes over Baja California in box shown in panel c). Dashed contours show climatological values, while colored contours indicate 2014 MHW anomalies.c) shows rainfall anomalies in the North American Regional Analysis, with stippling showing values that are not significant at the 95% level. d) shows the daily distribution of climatological (gray) and MHW (purple) summertime outgoing longwave radiation (OLR). Lower OLR values indicate cooler cloud tops on deep convective clouds. Gray bracket shows 95% CI for climatological values.

Supplementary Information for *Expansion and intensification of the North American Monsoon during the Pliocene*

Tripti Bhattacharya[1], Ran Feng[2], Jessica E. Tierney[3], Scott Knapp[4], Natalie Burls[4], and Minmin Fu[5]

[1]Department of Earth and Environmental Sciences, Syracuse University, NY, USA
[2]Department of Geosciences, University of Connecticut, CT, USA
[3]Department of Geosciences, University of Arizona, AZ, USA
[4]Department of Atmospheric, Oceanic and Earth Science, George Mason University, VA, USA
[5]Department of Earth and Planetary Sciences, Harvard University, MA, USA

April 13, 2022

Contents of this file

1 Figures and Tables

Table S1: Locations and interpretations of Pliocene data shown in Figure 1

Site No.	Name	Lat	Lon	Age Range (Ma)	Interpretation	Source
1	Diablo Formation	33.26	-116.37	3.8 - 2.6	mesic plant taxa including *Juglans, Carya, Umbellularia, Populus*	[1]
2	DSDP 467	33.83	-120.75	15 - 2.4	summer rain indicators like *Carya, Juglans* indicate summer wet to summer dry transition	[2]
3	Las Tunas	23.3	-109.7	4.75 - 2.6	faunal remains incl. *Crocodylus* and tortoise indicate perennial freshwater, tropical environment	[3]
4	Palm Springs Formation	33.57	-115.85	3.3 - 2.6	Lacustrine Deposits	Macrostrat, [4]
5	Gila Conglomerate	32.48	-108.26	4.0 - 2.6	Lacustrine Deposits	Macrostrat, [4]
6	Fort Hancock	31.91	-106.5	3.6 - 1.9	Lacustrine Deposits	Macrostrat, [4]
7	Santa Fe Group 1	33.05	-105.61	19.3 - 1.9	Lacustrine Deposits	Macrostrat, [4]
8	Santa Fe Group 2	34.15	-107.28	4.9 - 0.7	Lacustrine Deposits	Macrostrat, [4]
9	Sunshine Ranch/Saugus Fm	34.3	-118.53	3.1 - 2.8	Lacustrine Deposits	Macrostrat, [4]
10	Hueca Bolson, TX	30.90	-105.30	4.75 - 1.8	Lacustrine Deposits	Macrostrat, [4]
11	Hungry Valley	34.67	-118.66	4.9 - 2.6	Lacustrine Deposits	Macrostrat, [4]
12	Paso Robles	36.5	-121.74	1.9-8.3	Lacustrine Deposits	Macrostrat, [4]
13	Bidahochi	35.95	-109.91	2.6-5.3	Lacustrine Deposits	Macrostrat, [4]

Table S2: Age tie points used to construct chronologies for DSDP 475 and DSDP 36 in this study. For Age Marker types, LAD = last appearance datum; FAD = first appearance datum; T = top; B = bottom.

Site Name	Age (Ma)	Age Marker	Composite Depth (cm)
DSDP 475			
	0.42	*Stylatractus universus (Axoprunum angelinum), LAD [5]*	1436
	0.48	*Pseudoemiliana lacunosa, LAD [6]*	1793
	0.8-1.0	*Mesocena quadrangula, T [7]*	3291
	1.45	Change in radiolarian abundance [8]	5403
	1.8-1.9	*Discoaster brouweri, LAD [9]*	6321
	2.3-2.4	*Discoaster pentaradiatus, LAD [10, 9]*	6811
	2.4-2.5	*Discoaster surculus, LAD [10, 9]*	7621
	2.5-2.6	*Stichocorys peregrina, LAD [11]*	9481
	3.20	*Reticulofenestra psuedoumbilica LAD, Didymocyrtis avita (Panartatus avita) LAD[5]*	13031
	4.60	*Orthorhabdus (Ceratolithus) rugosus LAD [5]*	13327

Table S3: Individual plant taxa from the Arizona-Sonora Desert Museeum of δD_w and $\delta^{13}C$ for C_4 and C_3 taxa used to infer ε_{p-w}. δD_w values are based on the C-29 alkane. Graminoids marked with an asterisk (*). In the case of *Pedilanthus macrocarpus*, we report carbon isotope values of the C-31 n-alkane. In the case of *Solanum tridynamum* we report data from the C-30 alkanoic acid. For these taxa, no data from the C-29 alkane is available.

| Taxon	Ecosystem Type	Metabolic Pathway	$\delta^{13}C$ (‰VPDB)	δD_w (‰VSMOW)
Acacia willardiana	Thornscrub	C_3	no data	-92.9
Ambrosia ambrosoides	Sonoran Desert	C_3	-33.4	-148
Ambrosia cordifolia	Sonoran Desert	C_3	-36.5	-114
Ambrosia deltoidea	Sonoran Desert	C_3	-31.4	-143
*Aristida ternipes**	Sonoran Desert	C_4	-25.1	-166
Brongniartia tenuifolia	Thornscrub	C_3	no data	-131
Bursera fagaroides	Thornscrub	C_3	no data	-128
Bursera laxiflora	Thornscrub	C_3	-37.3	no data
Calliandra eriophylla	Sonoran Desert	C_3	-31.1	-103
*Cathestecum brevifolum**	Sonoran Desert	C_4	-24.1	-162
Dyschoriste hirsutissima	Thornscrub	C_3	no data	-141
Encelia farinosa	Sonoran Desert	C_3	-32.2	-166
Eupatorium sagittatum	Sonoran Desert	C_3	no data	-141.8
Forchhammeria watsonii	Thornscrub	C_3	no data	-106
Fouqueria macdouglaii	Thornscrub	C_3	no data	-131
Fouqueria splendens	Sonoran Desert	C_3	-30.6	-148
Guaiacum coulteri	Thornscrub	C_3	no data	-119
Haematoxylon brasilleto	Thornscrub	C_3	-31.9	-134
Ipomnea arborescens	Thornscrub	C_3	no data	-131
Jacquinia macrocarpa	Thornscrub	C_3	no data	-158
Janusia gracilis	Sonoran Desert	C_3	-34.4	-140.
Jatropha cartiophylla	Sonoran Desert	C_3	-29.9	-178
Larrea tridentata	Sonoran Desert	C_3	-30.7	-128
Melochia tomentosa	Thornscrub	C_3	no data	-143
*Muhlenbergia porterii**	Sonoran Desert	C_4	-22.9	-174
Olneya tesota	Sonoran Desert	C_3	-29.5	-122
Parkinsonia microphylla	Sonoran Desert	C_3	-30.8	-143
Pedilanthus macrocarpus	Sonoran Desert	CAM	-22.9	no data
Piscidia mollis	Sonoran Desert	C_3	no data	-125
Prosopis velutina	Sonoran Desert	C_3	-28.0	-125
Randia echinocarpa	Sonoran Desert	C_3	-28.0	-125
Simmondsia chinensis	Sonoran Desert	C_3	-30.3	-155
Solanum tridynamum	Thornscrub	C_3	no data	-150
Trixis californica	Sonoran Desert	C_3	-33.9	-158
Vachellia campechiana	Thornscrub	C_3	no data	-117
Vachellia constricta	Thornscrub	C_3	-37.7	-105
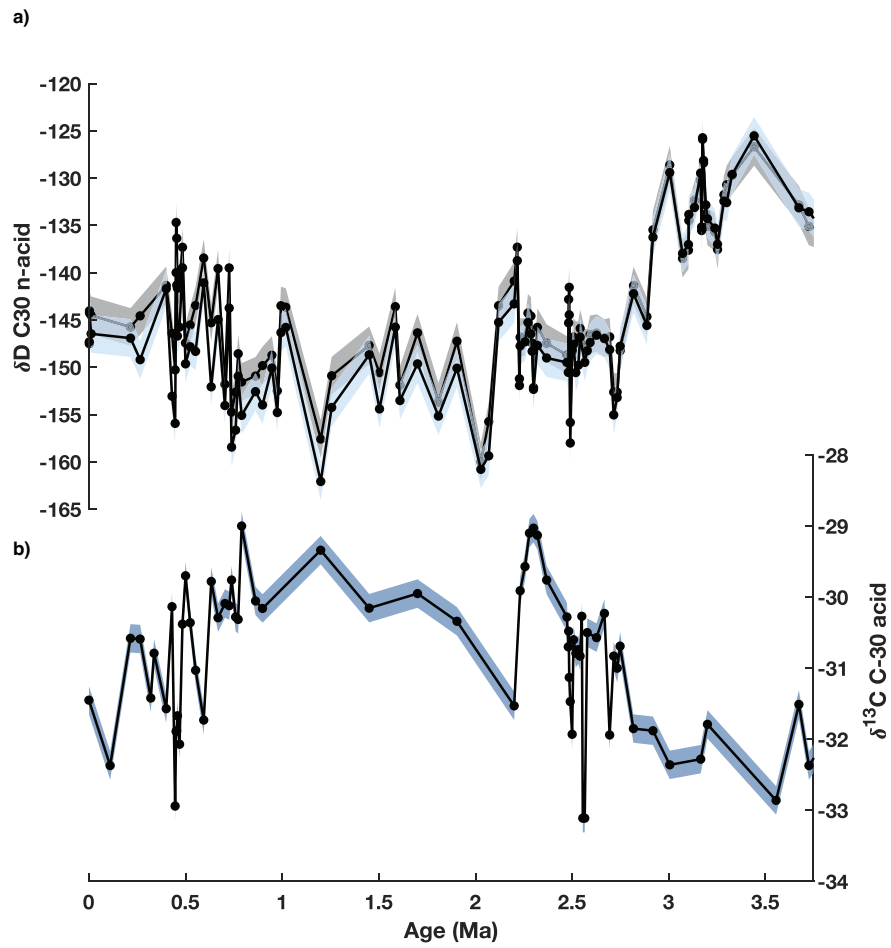
Figure S1: δD and δ^{13}C of the C-30 alkanoic acid from DSDP 475. a) shows the raw δD values with 1-σ analytical errors shown in green, as well as ice-volume corrected values with analytical errors in blue. The effect of a million-year ice volume correction is extremely minor. b) shows carbon isotope data with 1-σ analytical error. Note carbon isotopes are samples at a lower resolution since for several depths sample material was consumed for hydrogen isotope analysis.
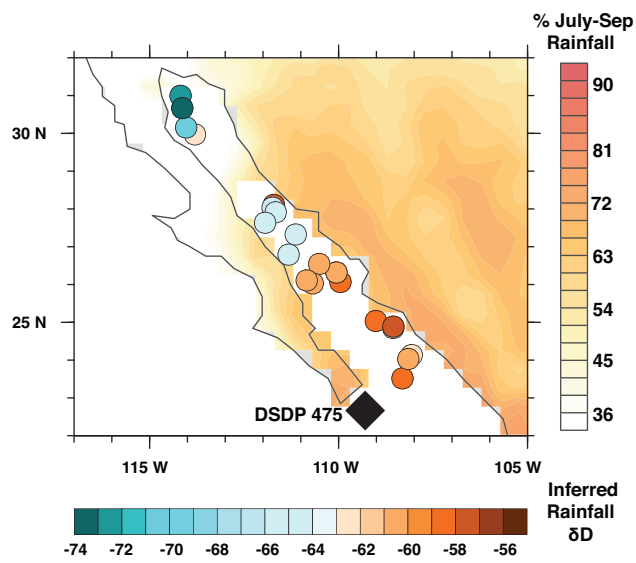
Figure S2: Coretop-inferred δD_p in the Gulf of California from [12]. Original data replotted using updated $\delta^{13}C$ and ε_{p-w} corrections from Table S3. Background contours indicate the importance of the NAM as a percentage of annual rainfall.
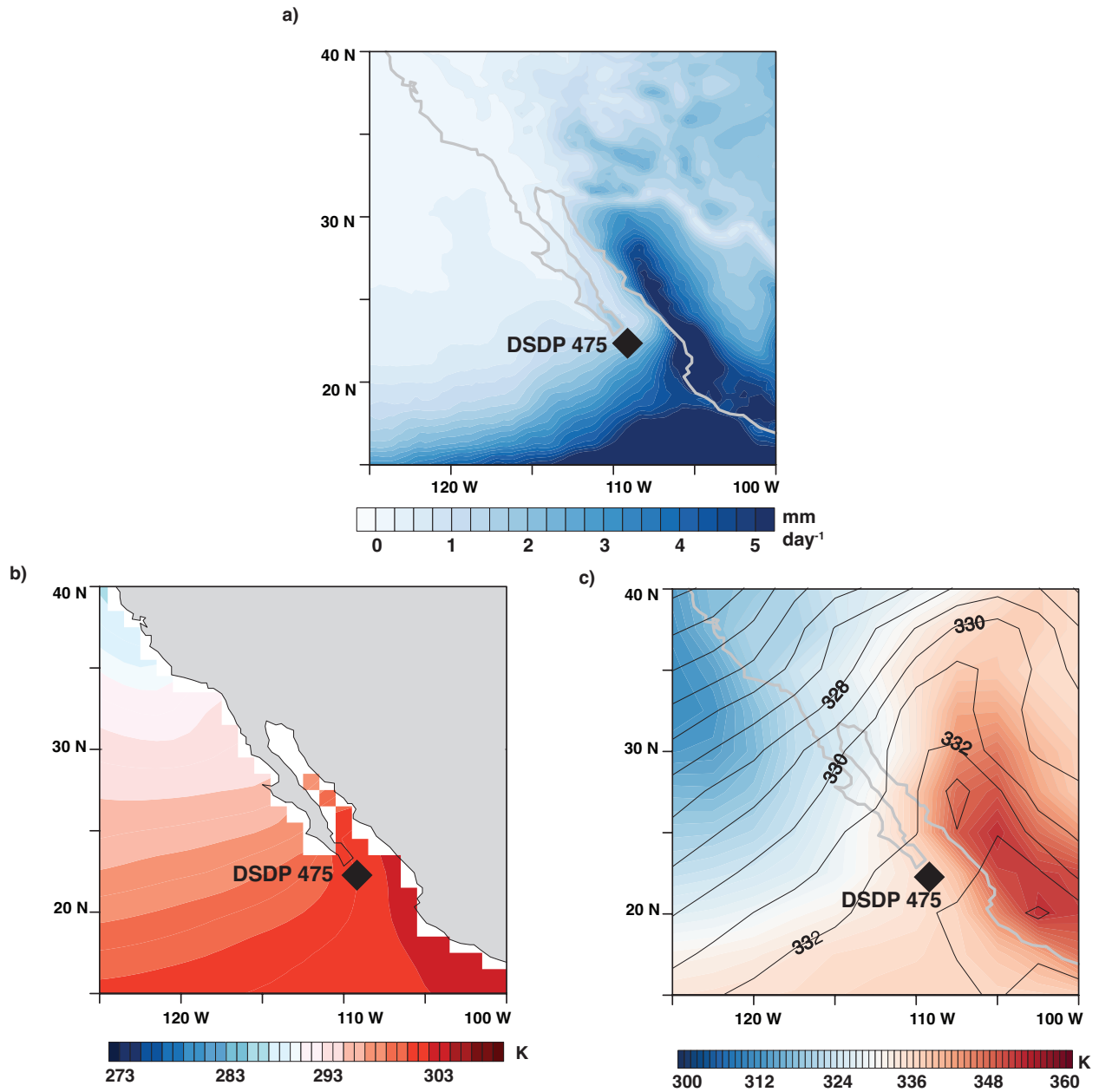
Figure S3: July-September climatology, calculated from 1950 - 2018, of a) rainfall in mm/day, b) sea surface temperatures, and c) equivalent potential temperature or θ_e (solid contours are mid-tropospheric or 400 mb θ_e, while colored contours are low-level (surface to 900 mb) average θ_e). The location of DSDP 475 is indicated on each plot.
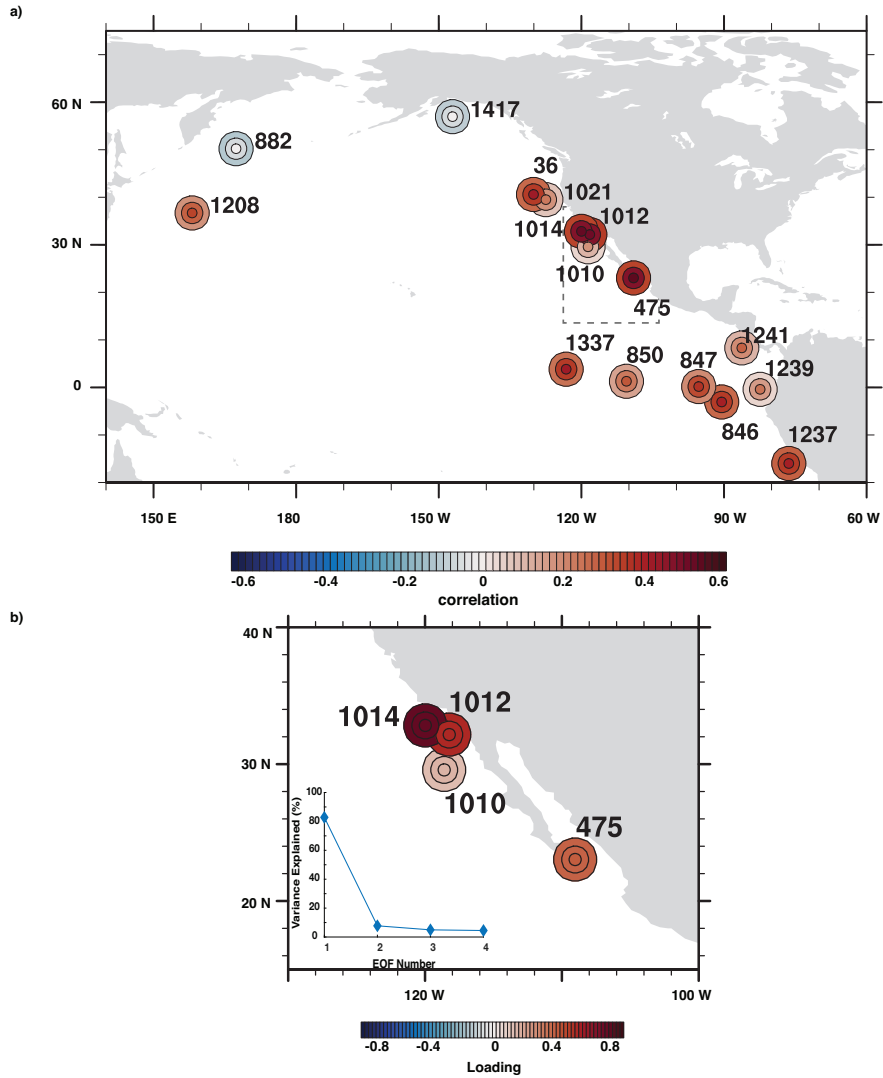
Figure S4: a) Correlation of δD_p from site 475 with continuous Plio-Pleistocene SST records. Inner circle represents upper 95% confidence interval, middle circle is median value, while outer circle is the lower 95% confidence interval of an ensemble of correlation estimates with analytical and calibration errors propagated through both timeseries. b) shows loadings onto individual sites for the EOF calculated on southern California margin Plio-Pleistocene SST records, with inset plot showing that this mode explains 83% of the variance.
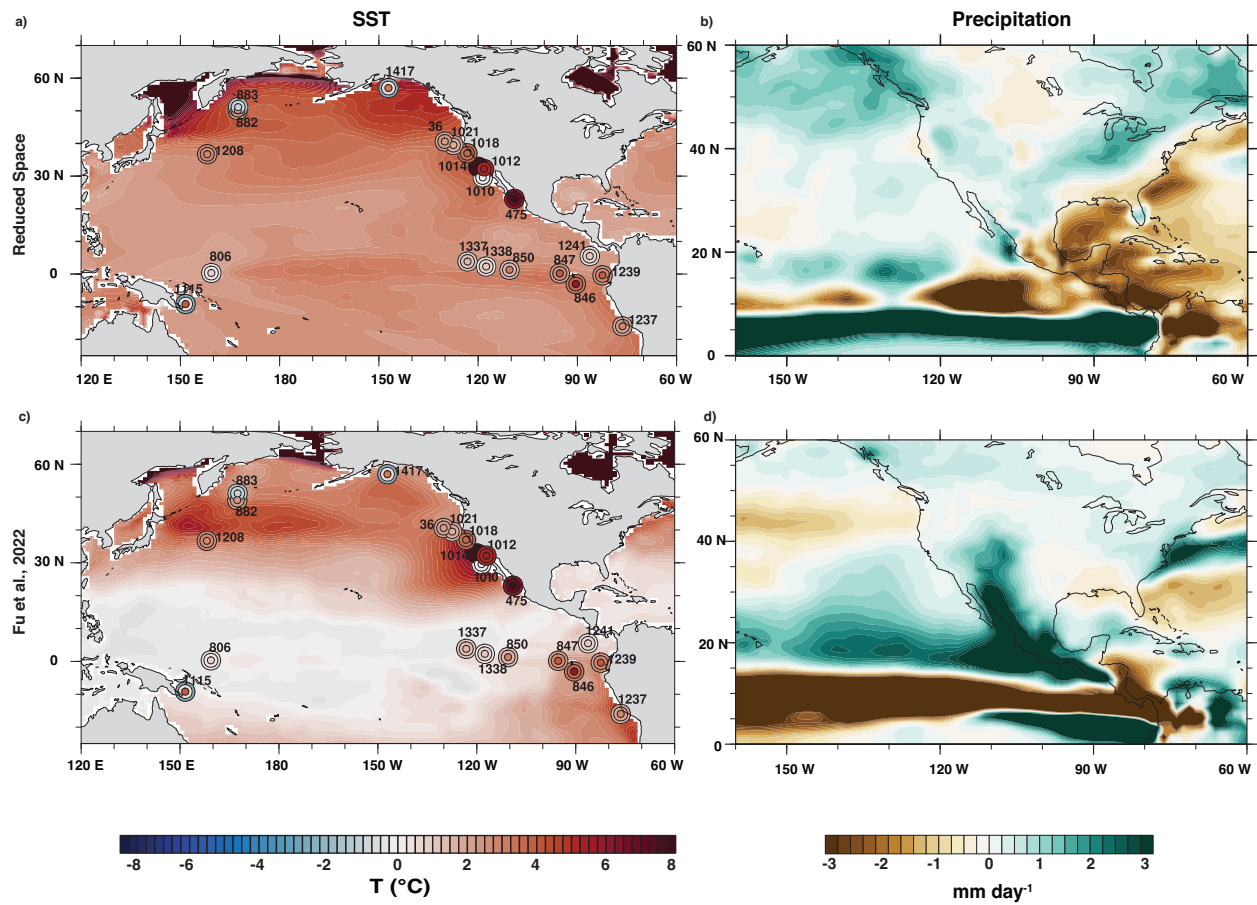
Figure S5: Climate changes in isotope-enabled simulations. Top row shows results for iCAM5 simulation forced with reduced space Pliocene SSTs anomalies, shown in main text. Bottom row shows results using SSTs from [13]. Panels a) and c) show SST changes, in comparison to available proxies. Panels b) and d)show summer precipitation changes. Site labels have been adjusted to improve visibility.
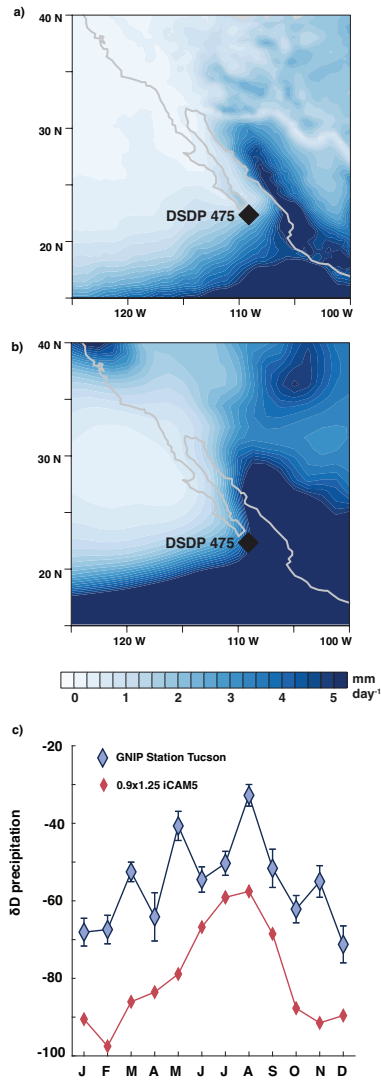
Figure S6: Observational vs. iCAM5 climatology for rainfall and seasonal cycle of isotopes. a) shows GPCP July-September rainfall [14].b) shows the model climatology for the same interval. c) shows the climatology and standard error of measured precipitation δD from the Tucson GNIP station [15] in dark blue compared to iCAM5's precipitation climatology for a region surrounding Tucson in red.
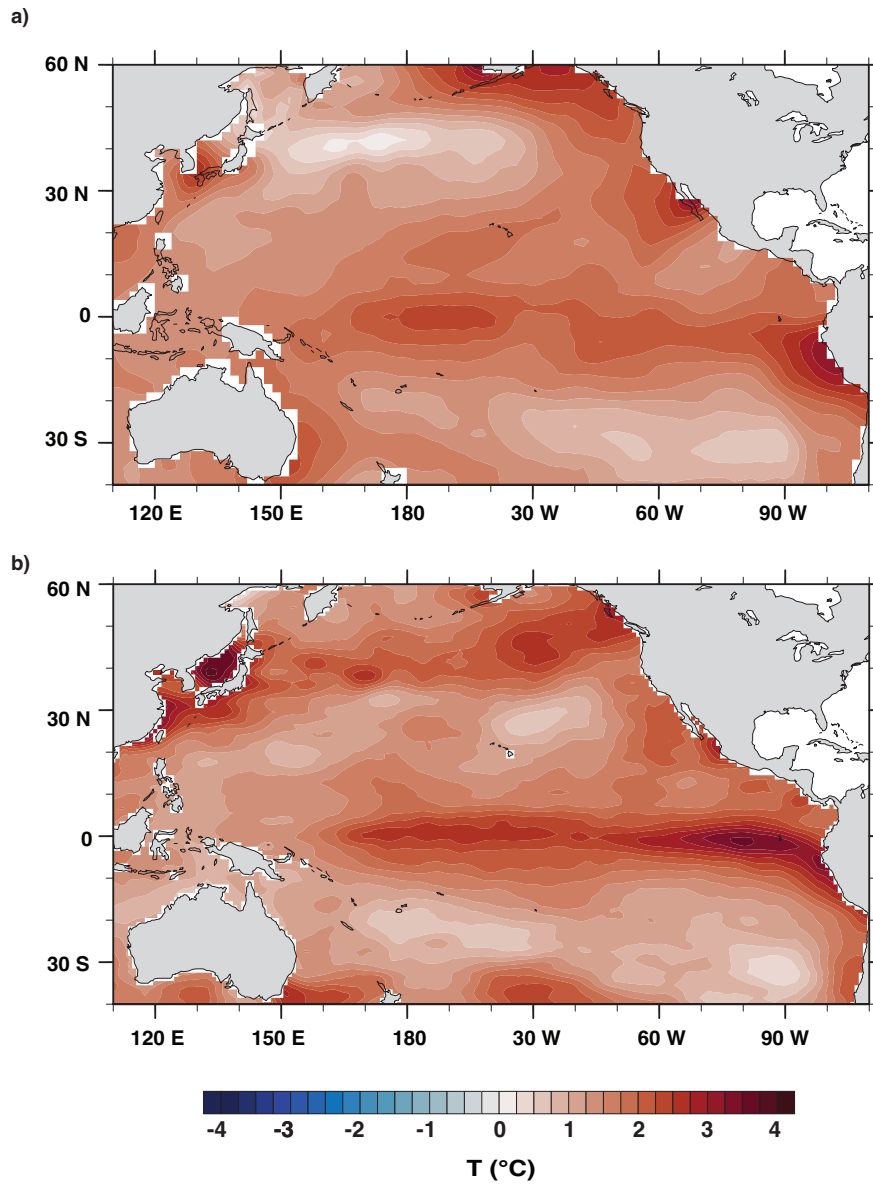
Figure S7: **Comparison of reduced space reconstructions of Pacific SSTs.**a) shows results from [16],which focused on the mid-Piacenzian interval, whereas b) shows results from our updated analyses using the COBE SST product [17] and focusing on the change between 5 -3 Ma.

References

[1] P. Remeika, I. W. Fischbein, S. A. Fischbein, Lower Pliocene petrified wood from the Palm Spring Formation, Anza Borrego Desert State Park, California. *Review of palaeobotany and palynology* **56**, 183–198 (1988).

[2] R. A. Ballog, R. E. Malloy, *Neogene Palynology from the Southern California Continental Borderland, Site 467, Deep Sea Drilling Project Leg 64*, vol. 63 of *Initial Reports of the Deep Sea Drilling Project, 63* (U.S. Government Printing Office, 1981).

[3] W. E. Miller, The late Pliocene Las Tunas local fauna from southernmost Baja California, Mexico. *Journal of Paleontology* pp. 762–805 (1980).

[4] D. E. Ibarra, *et al.*, Warm and cold wet states in the western United States during the Pliocene–Pleistocene. *Geology* **46**, 355–358 (2018).

[5] S. K. Haslett, Late Neogene-Quaternary radiolarian biostratigraphy: a brief review. *Journal of Micropalaeontology* **23**, 39–47 (2004).

[6] J. R. Young, Neogene nannofossils. *Calcareous Nannofossil Biostratigraphy. Kluwer Academic, Dordrecht* **225**, 265 (1998).

[7] D. Bukry, J. Foster, Silicoflagellate and diatom stratigraphy, Leg 16, Deep Sea Drilling Project. *Initial Reports of the Deep Sea Drilling Project* **16**, 815–871 (1973).

[8] A. Molina Cruz, Radiolarians in the gulf of california, deep sea drilling project leg 65. *Initial Reports of the Deep Sea Drilling Project* **64**, 983–1002 (1982).

[9] I. Raffi, *et al.*, A review of calcareous nannofossil astrobiochronology encompassing the past 25 million years. *Quaternary Science Reviews* **25**, 3113–3137 (2006).

[10] D. Bukry, Biostratigraphy of Cenozoic marine sediment by calcareous nannofossils. *Micropaleontology* pp. 44–60 (1978).

[11] J. Alexandrovich, Radiolarian biostratigraphy of odp leg 111, site 677, eastern equatorial pacific, late miocene through pleistocene. *Proceedings of the Ocean Drilling Program, Scientific Results (CD-ROM)* **111**, 245–262 (1989).

[12] T. Bhattacharya, J. E. Tierney, J. A. Addison, J. W. Murray, Ice-sheet modulation of deglacial North American monsoon intensification. *Nature Geoscience* **11**, 848–852 (2018).

[13] M. Fu, M. A. Cane, P. Molnar, E. Tziperman, Warmer Pliocene upwelling site SST leads to wetter subtropical coastal areas: a positive feedback on SST. *Paleoceanography and Paleoclimatology* p. e2021PA004357 (2022).

[14] R. F. Adler, *et al.*, The Global Precipitation Climatology Project (GPCP) monthly analysis (new version 2.3) and a review of 2017 global precipitation. *Atmosphere* **9**, 138 (2018).

[15] C. Eastoe, D. Dettman, Isotope amount effects in hydrologic and climate reconstructions of monsoon climates: Implications of some long-term data sets for precipitation. *Chemical Geology* **430**, 78–89 (2016).

[16] J. E. Tierney, A. M. Haywood, R. Feng, T. Bhattacharya, B. L. Otto-Bliesner, Pliocene warmth consistent with greenhouse gas forcing. *Geophysical Research Letters* **46**, 9136–9144 (2019).

[17] M. Ishii, A. Shouji, S. Sugimoto, T. Matsumoto, Objective analyses of sea-surface temperature and marine meteorological variables for the 20th century using icoads and the kobe collection. *International Journal of Climatology: A Journal of the Royal Meteorological Society* **25**, 865–879 (2005).